

# Improved sensitivity of cellular MRI using phase-cycled balanced SSFP of ferumoxytol nanocomplex-labeled macrophages at ultrahigh field

Yelong Shen,<sup>1,2</sup> Lirong Yan,<sup>1</sup>  
Xingfeng Shao,<sup>1</sup> Bin Zhao,<sup>2</sup>  
Jinlun Bai,<sup>3</sup> Wang Lu,<sup>3</sup> Danny  
JJ Wang<sup>1</sup>

<sup>1</sup>Laboratory of FMRI Technology (LOFT), Mark and Mary Stevens Neuroimaging and Informatics Institute, Keck School of Medicine, University of Southern California (USC), Los Angeles, CA, USA; <sup>2</sup>Shandong Medical Imaging Research Institute, School of Medicine, Shandong University, Jinan, Shandong, China; <sup>3</sup>Broad Center for Regenerative Medicine and Stem Cell Research, Keck School of Medicine, University of Southern California (USC), Los Angeles, CA, USA



Correspondence: Danny JJ Wang  
Laboratory of FMRI Technology (LOFT),  
Mark and Mary Stevens Neuroimaging and  
Informatics Institute, Keck School of Medicine,  
University of Southern California (USC), 2025  
Zonal Ave, Los Angeles, CA 90033, USA  
Tel +1 323 865 1730  
Email [jwang71@gmail.com](mailto:jwang71@gmail.com)

**Purpose:** The purpose of this study was to investigate the feasibility and sensitivity of cellular magnetic resonance imaging (MRI) with ferumoxytol nanocomplex-labeled macrophages at ultrahigh magnetic field of 7 T.

**Materials and methods:** THP-1-induced macrophages were labeled using self-assembling heparin + protamine + ferumoxytol nanocomplexes which were injected into a gelatin phantom visible on both microscope and MRI. Susceptibility-weighted imaging (SWI) and balanced steady-state free precession (bSSFP) pulse sequences were applied at 3 and 7 T. The average, maximum intensity projection, and root mean square combined images were generated for phase-cycled bSSFP images. The signal-to-noise ratio and contrast-to-noise ratio (CNR) efficiencies were calculated. Ex vivo experiments were then performed using a formalin-fixed pig brain injected with ~100 and ~1,000 labeled cells, respectively, at both 3 and 7 T.

**Results:** A high cell labeling efficiency (>90%) was achieved with heparin + protamine + ferumoxytol nanocomplexes. Less than 100 cells were detectable in the gelatin phantom at both 3 and 7 T. The 7 T data showed more than double CNR efficiency compared to the corresponding sequences at 3 T. The CNR efficiencies of phase-cycled bSSFP images were higher compared to those of SWI, and the root mean square combined bSSFP showed the highest CNR efficiency with minimal banding. Following co-registration of microscope and MR images, more cells (51/63) were detected by bSSFP at 7 T than at 3 T (36/63). On pig brain, both ~100 and ~1,000 cells were detected at 3 and 7 T. While the cell size appeared larger due to blooming effects on SWI, bSSFP allowed better contrast to precisely identify the location of the cells with higher signal-to-noise ratio efficiency.

**Conclusion:** The proposed cellular MRI with ferumoxytol nanocomplex-labeled macrophages at 7 T has a high sensitivity to detect <100 cells. The proposed method has great translational potential and may have broad clinical applications that involve cell types with a primary phagocytic phenotype.

**Keywords:** ultrasmall superparamagnetic iron oxide nanoparticles, ultrahigh field, balanced steady-state free precession, cellular magnetic resonance imaging, self-assembling nanocomplexes, 7 T

## Background

Noninvasive imaging of cells labeled with ultrasmall superparamagnetic iron oxide nanoparticles (USPIOs, <50 nm) in intact, live organisms has drawn growing interest in many fields related to cell transplantation, early detection of cell homing, and monitoring cell migration. During the past two decades, many studies have used magnetic resonance imaging (MRI) to track cells after they are labeled with USPIOs, including

stem cell tracking to damaged myocardium, early detection of tissue rejection, early detection of cancer and inflammation, and tracking neural stem cell response to stroke and trauma.<sup>1,2</sup> However, most cell-based imaging studies are preclinical with relatively few clinical studies in humans. In particular, there are several challenges for translating USPIO-based cellular MRI for in vivo human brain imaging: 1) MRI is typically described as having high image resolution, but low sensitivity (compared to positron emission tomography); reported sensitivity of human cellular MRI is generally on the order of a few thousand cells,<sup>3</sup> 2) gradient-echo (GRE) or T2\*-weighted sequences are typically used for detecting USPIO-labeled cells. The negative contrast of USPIOs on T2\*-weighted images may be confounded by other susceptibility effects, such as microhemorrhages, and is difficult to interpret in areas near air, bone, or areas with blood flow, and 3) the labeling efficiency of USPIOs is not high for most immune or stem cells, and the label will be diluted once the cell divides.

Recently, self-assembling nanocomplexes by combining three US Food and Drug Administration (FDA)-approved compounds – heparin, protamine, and ferumoxytol (HPF) – were introduced for efficient cell labeling with threefold increase in T2 relaxivity compared to ferumoxytol.<sup>4</sup> Here, we propose a novel method for cellular MRI using HPF nanocomplex-labeled white blood cells (macrophages) and phase-cycled balanced steady-state free precession (bSSFP) sequences at ultrahigh field (UHF) of 7 T. This method is expected to effectively address the limitations of existing USPIO-based cellular MRI while retaining the high spatial resolution and contrast for the visualization of brain anatomy and function. As a proof-of-concept, we demonstrate the feasibility and evaluate the sensitivity of this technique in in vitro studies and ex vivo brain specimen at both 3 and 7 T.

## Materials and methods

The present study was exempt from Institutional Animal Care and Use Committee approval as no vertebrate animal was involved in the experiment. Figure 1 shows the schematic diagram of the workflow of our study, including nanocomplex preparation, cell labeling and staining, labeling verification by microscope followed by MRI of labeled cells in phantom and ex vivo tissue samples. Below we describe the detailed methods for each step.

### Cell preparation

THP-1 is a human promonocytic cell line derived from acute monocytic leukemia.<sup>5</sup> THP-1 cells (American Type Culture Collection) were maintained at 37°C and 5% CO<sub>2</sub>

in RPMI 1640 (Thermo Fisher Scientific, Waltham, MA, USA) supplemented with 10% fetal bovine serum (FBS; Thermo Fisher Scientific), 1% penicillin/streptomycin, and 10 mM HEPES (Calbiochem). Also, 100 ng/mL of phorbol 12-myristate 13-acetate was added and incubated for 3 days to convert THP-1 cells into phagocytic macrophage cells.

### Cell labeling

Adherent monolayer THP-1-differentiated macrophages were grown to 80%–90% confluence. The macrophages were then labeled in serum-free RPMI-1640. Different labeling strategies and labeling times (1 and 2 days) were tested on the THP-1 differentiated macrophages, including 1) ferumoxytol (Feraheme®; AMAG Pharmaceuticals, Boston, MA, USA) only, 2) ferumoxytol + protamine, and 3) HPF (Figure 2), which were used to label the cells to achieve a high labeling efficiency and T2 relaxivity. The concentrations of ferumoxytol, protamine, and heparin in each labeling condition were kept the same: heparin (2 IU/mL), protamine (60 µg/mL), and ferumoxytol (50 µg/mL). The three compounds were mixed together to form self-assembling nanocomplexes for 5 min according to Thu et al.<sup>4</sup> After incubation in serum-free medium for 2–4 hours, FBS was added to make the concentration of FBS 10%–20% in the medium. The three USPIO compounds were added into the corresponding medium, respectively, and incubated 1 or 2 days, respectively. Adhered macrophages were then detached from incubation with pancreatic enzymes (0.25%) combined with EDTA (1 mM) and then washed in PBS for three times. Cell number was counted by a hemocytometer twice to obtain the average number.

### Cell viability and labeling efficiency

Cell viability was then confirmed by the trypan blue exclusion test for membrane integrity according to a published protocol.<sup>6</sup> Cells were counted using a cell counting chamber. A cell viability of >90% was the criterion for the following steps.

The labeled cells were stained by Prussian blue to verify the labeling efficiency. Perls' Prussian blue staining was applied for displaying ferric iron and ferritin protein.<sup>7</sup> After labeling with three compounds of ferumoxytol for 1 or 2 days, the labeled cells were fixed with 4% paraformaldehyde for 5 min. A mixture of 4% potassium ferrocyanide (potassium hexacyanoferrate (II) trihydrate, Sigma) and 3.7% hydrochloric acid (Perls' reagent for Prussian blue staining) was added for 30 min, and then cells were washed with PBS for three times.

Finally, the stained cells were imaged and captured using a phase-contrast reverse microscope (20×; Leica Microsystems, Wetzlar, Germany). Cells exhibiting blue intracellular

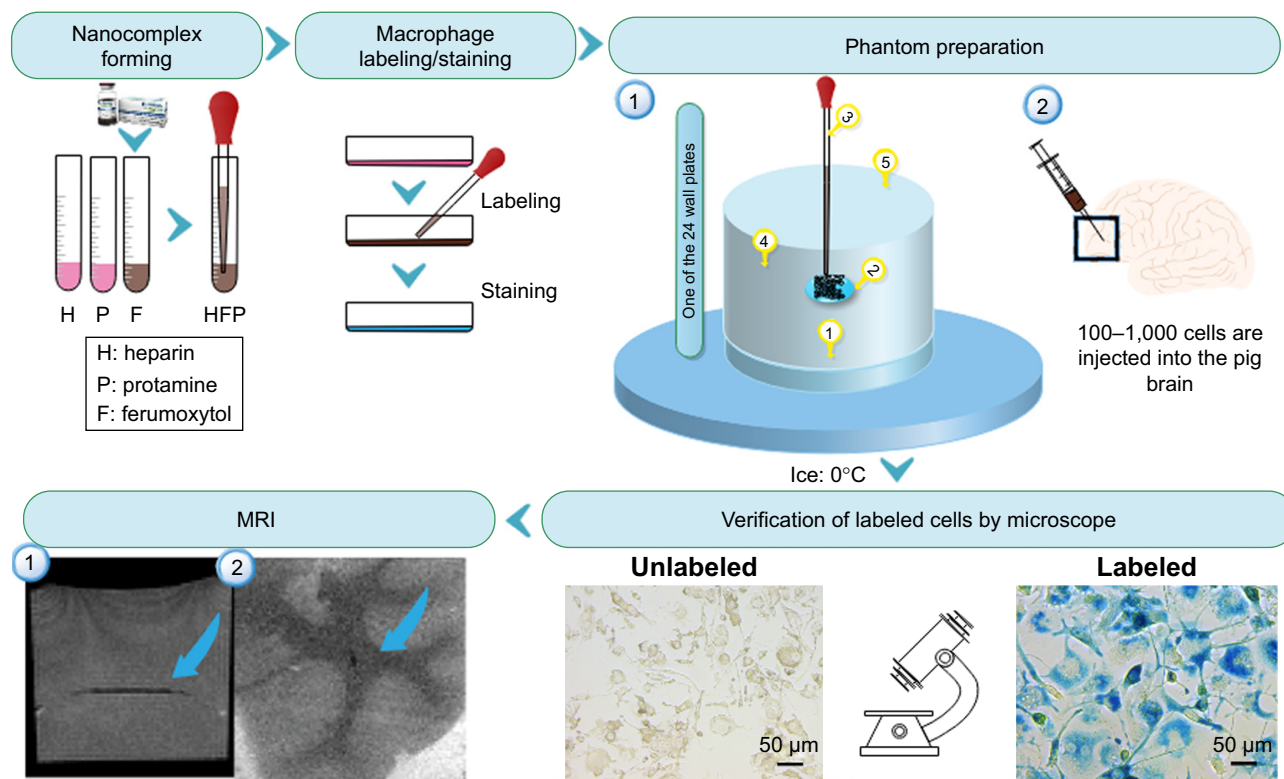


**Figure 1** Schematic diagram of the workflow to show the process of nanocomplex preparation, cell labeling, cell staining, labeling verification by microscope, and MRI. **Notes:** Numbers in phantom preparation indicate as (1) adding 200  $\mu\text{L}$  4% gelatin at the bottom of each well; (2) adding 100  $\mu\text{L}$  4% gelatin in the middle of each well and on top of the solid layer formed by the 200  $\mu\text{L}$  gelatin of step 1; (3) injecting 10  $\mu\text{L}$  media with labeled cells and 10% trypan blue in the middle of the previously added 100  $\mu\text{L}$  4% gelatin before it was frozen; (4) filling the tube with 4% gelatin after the gelatin turned solid and the cells were fixed; (5) removing air bubbles in gelatin using a pipette. Images in MRI represent (1) MRI image of labeled cells in a gel phantom; (2) MRI image of labeled cells in ex vivo pig brain tissue. Blue arrows represent location of labeled cells. Magnification 5 $\times$ 20 for images from verification of labeled cells by microscope. **Abbreviation:** MRI, magnetic resonance imaging.

particles were considered Prussian blue positive. The percentage of labeled cells was determined from the average of the labeled cells versus the total number of cells from four randomly selected fields of view.

### Gelatin phantom preparation

A gelatin phantom was designed and constructed to be suitable for both microscope imaging and MRI using 24-well plates (Figure 3). Five steps were followed as shown in Figure 1: 1) adding 200  $\mu\text{L}$  4% gelatin at the bottom of each well; 2) adding 100  $\mu\text{L}$  4% gelatin in the middle of each well and on the top of the solid layer formed by the 200  $\mu\text{L}$  gelatin of Step 1; 3) injecting 10  $\mu\text{L}$  media with labeled cells and 10% trypan blue in the middle of the previously added 100  $\mu\text{L}$  4% gelatin before it was frozen; 4) filling the tube with 4% gelatin after the gelatin turned solid and the cells were fixed; and 5) removing air bubbles in gelatin using a pipette.

The central eight wells of the 24-well plate were prepared as above, and the remaining 16 wells were directly injected with 4% gelatin as control. The phantom was stored in a

refrigerator at 4°C for MRI the next day. Several (six to eight) 24-well plates were stacked for MRI (Figure 3).

The labeled cells were diluted to concentrations of 6.20 $\times$ 10<sup>3</sup>/mL, 1.25 $\times$ 10<sup>4</sup>/mL, 2.50 $\times$ 10<sup>4</sup>/mL, 5.00 $\times$ 10<sup>4</sup>/mL, and 1.00 $\times$ 10<sup>5</sup>/mL. Then, 10  $\mu\text{L}$  cell solutions with concentrations of 6.20 $\times$ 10<sup>3</sup>/mL, 1.25 $\times$ 10<sup>4</sup>/mL, 2.50 $\times$ 10<sup>4</sup>/mL, 5.00 $\times$ 10<sup>4</sup>/mL, and 1.00 $\times$ 10<sup>5</sup>/mL were injected into the gelatin phantom. Hence, the wells of the gelatin phantom contained ~62, 125, 250, 500, and 1,000 cells in 10  $\mu\text{L}$  medium.

### Brain specimen preparation

A fresh pig brain was purchased from the supermarket, incubated, and fixed with formalin. The HPF-labeled cells were diluted to a concentration of 1 $\times$ 10<sup>5</sup>/mL, and then, 1  $\mu\text{L}$  and 10  $\mu\text{L}$  solutions were injected into the pig brain cortex. Hence, ~100 and 1,000 cells were injected with a microinjection needle into the pig brain cortex. Right before injection, the needle was pulled back 1 mm, and the cells were administered at a rate of 0.5  $\mu\text{L}$  per 2 min to prevent reflux. For MRI, the pig brain was cut into several pieces to fix in

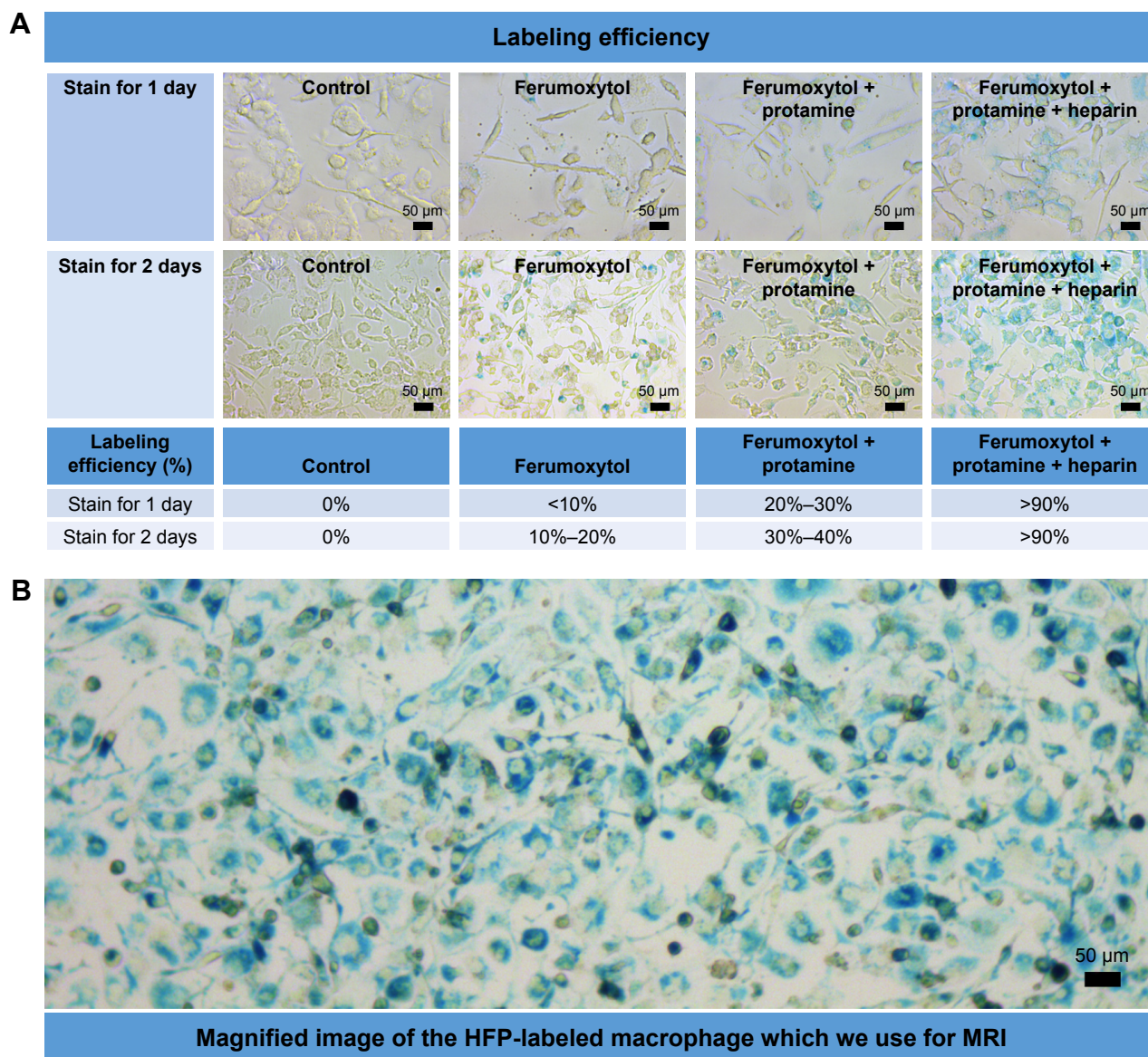


**Figure 2 (A)** Labeling efficiency of different labeling methods. The labeling efficiency of ferumoxytol only (<20%) or combining ferumoxytol and protamine (<40%) was relatively poor, while self-assembling nanocomplexes formed by combining ferumoxytol, heparin, and protamine could achieve a high labeling efficiency (>90%). **(B)** Magnified image of HPF-labeled macrophage stain used for MRI. Magnification 5×20.

**Abbreviations:** HPF, heparin, protamine, and ferumoxytol; MRI, magnetic resonance imaging.

a small plastic box and submerged in formalin. This step minimized susceptibility artifacts due to air bubbles.

## MRI of labeled cells

All MR images were acquired on a 3 T Prisma and a 7 T Terra whole-body MR system (Siemens, Erlangen, Germany) with 32-channel head coils. Two MRI pulse sequences using susceptibility-weighted imaging (SWI) and bSSFP were applied with an identical spatial resolution of  $0.2 \times 0.2 \times 0.2 \text{ mm}^3$  and closely matched imaging parameters, as shown in Table 1. The imaging protocols were based on literature<sup>8</sup> as well as our empirical testing

and practical constrain of scan time. For instance, SWI scans had four measurements in order to achieve adequate image quality at 3 T, while only two measurements were needed at 7 T. The differences in imaging time were accounted for during post-processing (see below). To minimize the banding artifact in bSSFP, phase cycling was performed with a total step of 16 (phase shift of  $\pi/8$ ).<sup>8</sup> In addition, standard single-phase bSSFP scans were performed with identical parameters of phase-cycled bSSFP without phase shift. Details of the imaging parameters of SWI, bSSFP, and phase-cycled bSSFP are listed in Table 1.

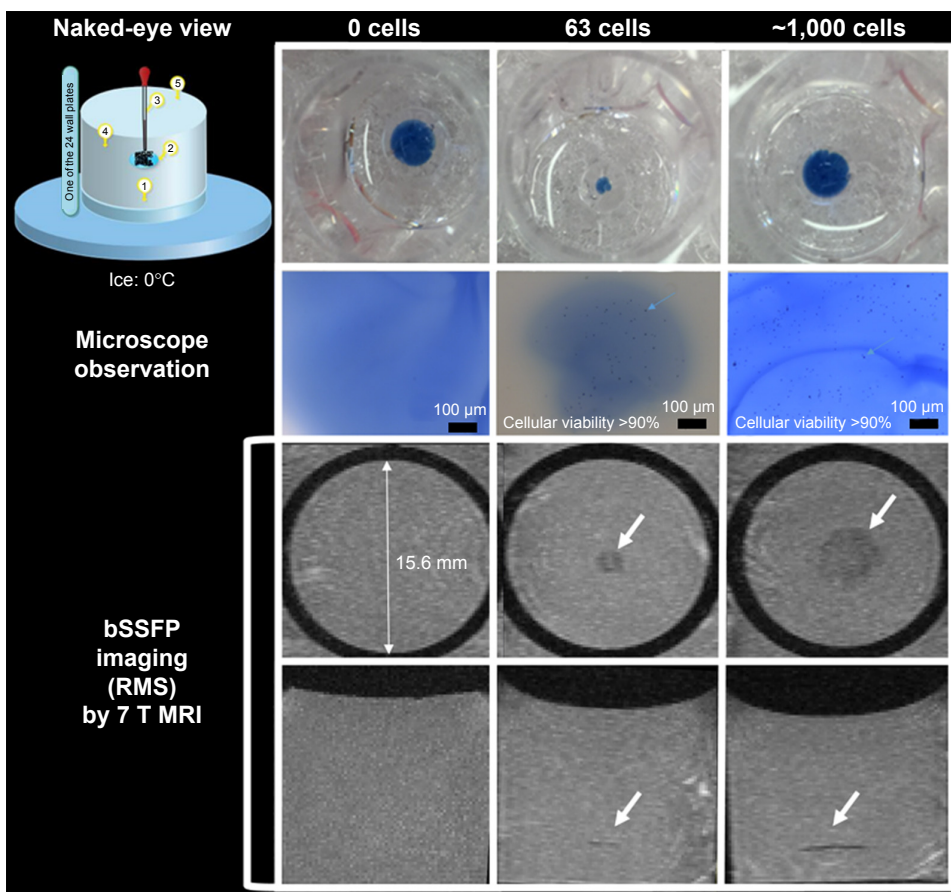


**Figure 3** Diagram showing phantom preparation method by fixing macrophages between two layers of gelatin without air bubbles. **Notes:** Numbers in naked-eye view image indicate as (1) adding 200  $\mu$ L 4% gelatin at the bottom of each well; (2) adding 100  $\mu$ L 4% gelatin in the middle of each well and on top of the solid layer formed by the 200  $\mu$ L gelatin of step 1; (3) injecting 10  $\mu$ L media with labeled cells and 10% trypan blue in the middle of the previously added 100  $\mu$ L 4% gelatin before it was frozen; (4) filling the tube with 4% gelatin after the gelatin turned solid and the cells were fixed; (5) removing air bubbles in gelatin using a pipette. Both microscope (top row, dark dots are individual cells) and MRI (second and third rows showing sagittal and axial views of RMS combined bSSFP images) can be used to image the phantom. A cellular level of <100 cells can be achieved with this phantom and can be clearly detected by MRI with RMS combined phase-cycled bSSFP images. White arrows show the location of the labeled cells. **Abbreviations:** bSSFP, balanced steady-state free precession; MRI, magnetic resonance imaging; RMS, root mean square.

### Post-processing of MRI

The phase-cycled bSSFP images were processed by three methods with a custom Matlab program: 1) average of the signal (AVE), 2) maximum intensity projection (MIP),

and 3) root mean square (RMS) of images across phase cycles. Both signal-to-noise ratio (SNR) efficiency and contrast-to-noise ratio (CNR) efficiency were calculated for three times for the phantom study and the ex vivo brain

**Table 1** Parameters of SWI, bSSFP, and phase-cycled bSSFP for MRI scan of the gelatin phantom and brain specimen at 3 and 7 T

Sequences	3 T		7 T	
	SWI	Phase-cycled bSSFP ( $\times 16$ )	SWI	Phase-cycled bSSFP ( $\times 16$ )
FOV (mm)	120	120	120	120
Resolution (mm <sup>3</sup> )	0.2 $\times$ 0.2 $\times$ 0.2	0.2 $\times$ 0.2 $\times$ 0.2	0.2 $\times$ 0.2 $\times$ 0.2	0.2 $\times$ 0.2 $\times$ 0.2
TR (ms)	29	12	25	9
TE (ms)	16	6	14	4
FA	15°	40°	15°	33°
Bandwidth (Hz/Px)	120	279	130	276
Measurement	4	16	2	16
Total scan time (min)	107	61	40	59

**Abbreviations:** bSSFP, balanced steady-state free precession; FA, flip angle; FOV, field of view; MRI, magnetic resonance imaging; SWI, susceptibility-weighted imaging; TE, echo time; TR, repetition time.

**Table 2** SNR and CNR efficiencies of SWI/bSSFP images acquired at 3 and 7 T on 1,000 cells injected into the gelatin phantom

Imaging sequences	SNR efficiency		CNR efficiency	
	3 T	7 T	3 T	7 T
SWI	1.04	3.18	0.19	0.41
bSSFP (2 average)	2.68	10.64	0.21	1.06
bSSFP (4 average)	2.40	8.99	0.55	1.36
AVE	2.64	7.63	0.86	2.88
MIP	1.43	3.33	0.65	1.08
RMS	2.71	6.17	1.02	3.48

**Note:** SNR and CNR efficiencies were calculated from regions of interest without banding artifacts.

**Abbreviations:** AVE, average of the signal; bSSFP, balanced steady-state free precession; CNR, contrast-to-noise ratio; MIP, maximum intensity projection; RMS, root mean square; SNR, signal-to-noise ratio; SWI, susceptibility-weighted imaging.

study, and the mean values are reported in Tables 2 and 3, respectively.

The SNR efficiency was defined as:

$$\eta_{\text{SNR}} = \frac{S_A}{\sqrt{\text{Tacq}} \sigma_0}$$

where  $S_A$  is the mean signal intensity of the phantom or brain tissue region without cell or artifact and  $\sigma_0$  is the SD of the background noise. Tacq is the image acquisition time.

The CNR efficiency was defined as:

$$\eta_{\text{CNR}} = \frac{|S_A - S_B|}{\sqrt{\text{Tacq}} \sigma_0}$$

where  $S_A$  and  $S_B$  are the signal intensities of the region with injected cells and surrounding region without cell or artifact, respectively.

MRI signal changes of bSSFP and SWI at 3 and 7 T as a function of the injected cell number were measured on gelatin phantom and ex vivo brain specimen, respectively. Furthermore, the volumes of the labeled cells were manually

segmented by ITK-SNAP.<sup>9</sup> The segmented volume and the SNR and CNR efficiencies were calculated for three times and the mean values were reported. Furthermore, image co-registration between microscope and MRI was performed using b-spline transformation and mutual information metric provided in Elastix.<sup>10</sup> This step allowed verification of the detection of <100 cells using MRI.

## Evaluation of reproducibility

The phantom was constructed three times following the identical procedures as described above, and MR images (both 3 and 7 T) were acquired the following day. Statistical analysis was performed using GraphPad Prism 5 software (GraphPad Software, Inc.), and a  $p$ -value  $\leq 0.05$  (two-sided) was considered statistically significant.

## Results

### Cell labeling efficiency

As shown in Figure 2 of cell staining results, cell labeling using HPF nanocomplexes achieved a high labeling efficiency of >90% for both 1 and 2 days of labeling. The other two labeling methods were much less efficient (ferumoxyl <20% and <10%, ferumoxyl + protamin <40% and 30% for labeling time of 2 and 1 day, respectively). We chose cell labeling with HPF nanocomplexes for 2 days in the following experiments to achieve the highest labeling efficiency.

### MRI with SWI, bSSFP, and phase-cycled bSSFP in gelatin phantom

Figure 3 shows the gelatin phantom by fixing macrophages between two layers of gelatin without air bubbles. Both microscope (top row, dark dots are individual cells) and MRI (second and third rows showing sagittal and axial views of RMS combined bSSFP images) can be applied to image the phantom. A cellular level of <100 cells can be

**Table 3** SNR and CNR efficiencies and segmented volumes of 100 and 1,000 labeled cells in a brain specimen using SWI and RMS combined phase-cycled bSSFP by 3 and 7 T

Number and concentration of the cells	Field strength MRI sequence	3 T			7 T		
		Volume (mm <sup>3</sup> )	SNR	CNR	Volume (mm <sup>3</sup> )	SNR	CNR
100 cells	SWI	0.6	0.26	0.09	0.62	1.71	0.85
1,000 cells	SWI	1.62	0.2	0.31	1.89	1.48	1.07
100 cells	bSSFP	0.31	1.59	0.42	0.41	2.56	1.04
1,000 cells	bSSFP	0.81	1.29	0.52	1.04	2.89	1.32

**Abbreviations:** bSSFP, balanced steady-state free precession; CNR, contrast-to-noise ratio; MRI, magnetic resonance imaging; RMS, root mean square; SNR, signal-to-noise ratio; SWI, susceptibility-weighted imaging.

achieved with this phantom and can be clearly detected by MRI with phase-cycled bSSFP images. The cells were intact in the gelatin phantom as shown by the microscope images (second row of Figure 3).

Figure 4 shows a comparison of SWI and bSSFP images of the gelatin phantom with ~1,000 labeled cells at 3 T (top row) and 7 T (bottom row), respectively. The original single-phase bSSFP images show banding artifacts, which are severer in images with four averages compared to those with two averages, due to magnetic field drift with time, especially at 7 T. The banding artifacts are suppressed in AVE, MIP, and RMS combined phase-cycled bSSFP images. The SNR and CNR efficiency values are listed in Table 2. At the same field strength, the SNR efficiencies of phase-cycled and single-phase bSSFP are higher than that of SWI. The CNR efficiencies are the highest using RMS and AVE combined phase-cycled bSSFP, followed by MIP combined phase-cycled bSSFP and standard single-phase bSSFP, and the lowest in SWI. Both SNR and CNR efficiencies are approximately doubled or more than doubled at 7 T compared to those at 3 T.

Figure 5 shows the results of SWI and RMS combined bSSFP imaging of different cell concentrations (~62, 125, 250, 500, and 1,000 cells in 10  $\mu$ L medium) at 3 and 7 T, respectively. The three-dimensional rendering of manually segmented volume of labeled cells (using ITK-SNAP) with different concentrations of cells using SWI and bSSFP are shown in Figure 6. Phase-cycled bSSFP images with three different combination methods (AVE, MIP, and RMS) at 3 and 7 T are shown in Figure S1.

As shown in Figure 5, the CNR efficiency increases as the number of labeled cells increases. CNR efficiency is  $>1$  for all cell concentrations using bSSFP at 7 T, while it is  $>1$  only for 1,000 cells in 10  $\mu$ L condition using bSSFP at 3 T. For SWI, the CNR efficiencies are below 0.6 for all cell concentrations at 3 and 7 T. Also, the segmented volume of labeled cells increases as the cell number increases. The segmented volume of the cells is generally larger in SWI compared to that of bSSFP due to the stronger blooming effect of SWI. However, the segmented volume of 62 labeled cells is comparable between bSSFP and SWI.

## Comparison of MRI and microscope

Figure 7 shows the co-registration of microscope images and RMS combined bSSFP MRI of the phantom with 63 labeled cells. More cells (51/63, 81%) were detected in 7 T images compared to 3 T (36/63, 57%) with a threshold of 40% signal decrease. SWI is also shown in Figure 7, which is deemed too noisy for image registration.

## SWI and bSSFP MRI of labeled cells in brain specimen

As shown in Figure 8, ~100 and ~1,000 cells can be imaged by both bSSFP and SWI in a brain specimen with 3 and 7 T scanners. The volume and the SNR and CNR efficiencies are listed in Table 3. For SNR and CNR, the 7 T scanner has better performance than the 3 T scanner while bSSFP has better performance than SWI. The volume of segmented cells is larger by SWI compared to that by bSSFP, which may be the result of the blooming effect of SWI.

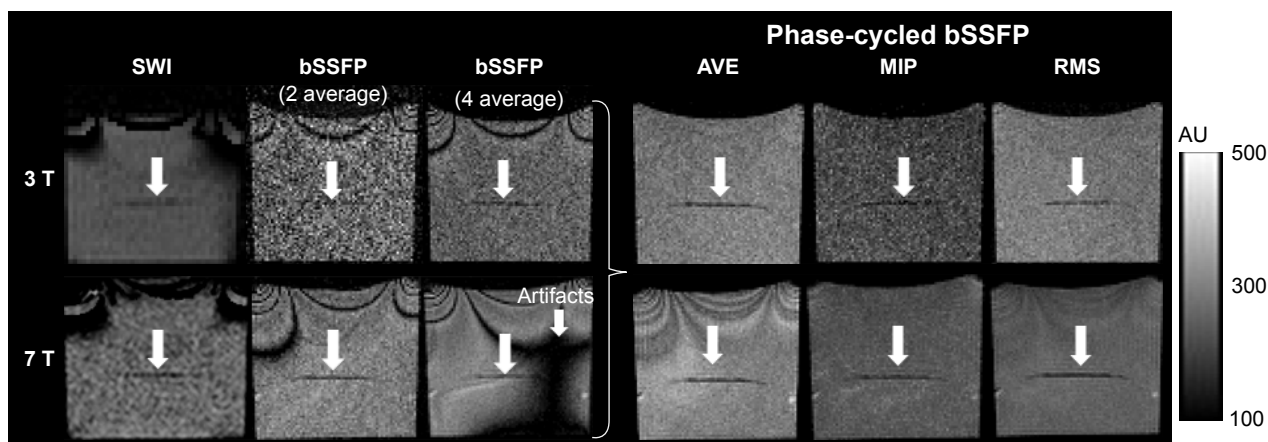


**Figure 4** Comparison of SWI and bSSFP images of phantom with ~1,000 labeled cells at 3 T (top row) and 7 T (bottom row).

**Notes:** The original bSSFP images show banding artifacts which are suppressed in combined phase-cycled AVE, MIP, and RMS images. Severer banding artifact in bSSFP images with four averages is due to magnetic field drift with time. White arrows show the location of labeled cells.

**Abbreviations:** AVE, average of the signal; bSSFP, balanced steady-state free precession; MIP, maximum intensity projection; RMS, root mean square; SWI, susceptibility-weighted imaging.

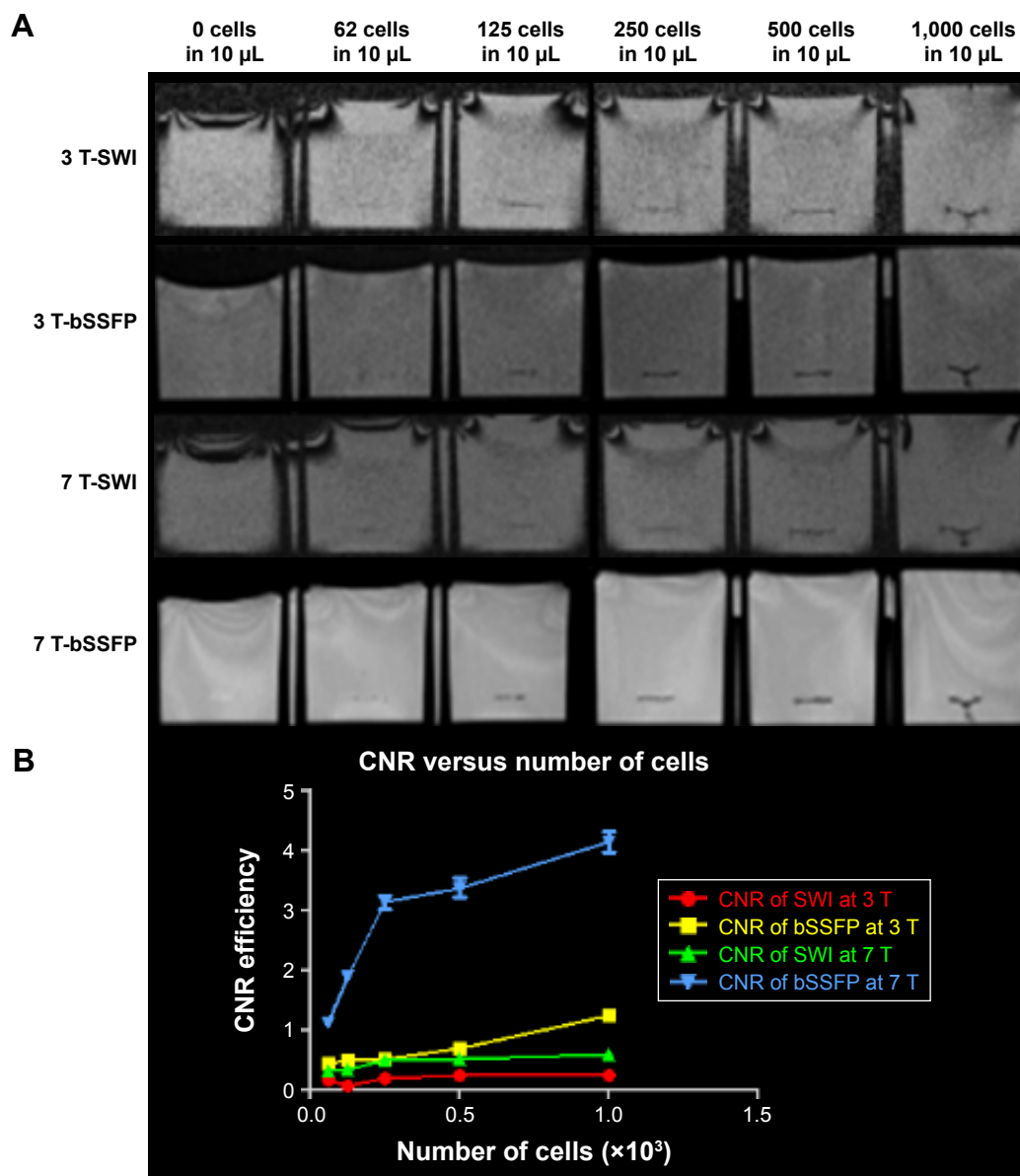


**Figure 5 (A)** SWI and RMS combined phase-cycled bSSFP images of different concentrations of cells (about 0, 62, 125, 250, 500, and 1,000 cells in 10  $\mu\text{L}$  medium) injected into the gelatin phantom at 3 and 7 T. **(B)** CNR efficiency of MRI versus number of cells using SWI, RMS bSSFP at 3 and 7 T.

**Abbreviations:** bSSFP, balanced steady-state free precession; CNR, contrast-to-noise ratio; MRI, magnetic resonance imaging; RMS, root mean square; SWI, susceptibility-weighted imaging.

## Discussion

### SSFP imaging for detecting USPIO-labeled cells

Using combined phase-cycled bSSFP, <100 cells were detected in a gelatin phantom at both 3 and 7 T using clinical MRI scanners and product 32-channel head coils in the present study. The majority of earlier studies examined a relatively large number of cells ( $10^5$ – $10^6$  cells).<sup>11</sup> Recent studies have moved toward detecting a smaller number of cells or even single cells. Hoehn et al<sup>12</sup> demonstrated an in vivo detection limit of 500 stem cells implanted in the rat brain. Dahnke and

Schaeffter<sup>13</sup> predicted the detection limit to be 600 labeled cells per voxel in the brain and 28,000 labeled cells per voxel in the liver using 3 T MRI. Kircher et al<sup>14</sup> showed that as few as three USPIO-labeled cytotoxic lymphocytes per voxel could be detected at 8.5 T in a tumor in live mice. Single SPIO-labeled cells have been reported to be detectable in in vitro studies at both low field strength (1.5 T with a custom gradient coil)<sup>15</sup> and UHF strength (7 T)<sup>16,17</sup> animal scanner. However, to the best of our knowledge, the minimal number of USPIO-labeled cells reported in literature imaged by clinical MRI scanners and coils was ~1,000 cells.<sup>4,18</sup>



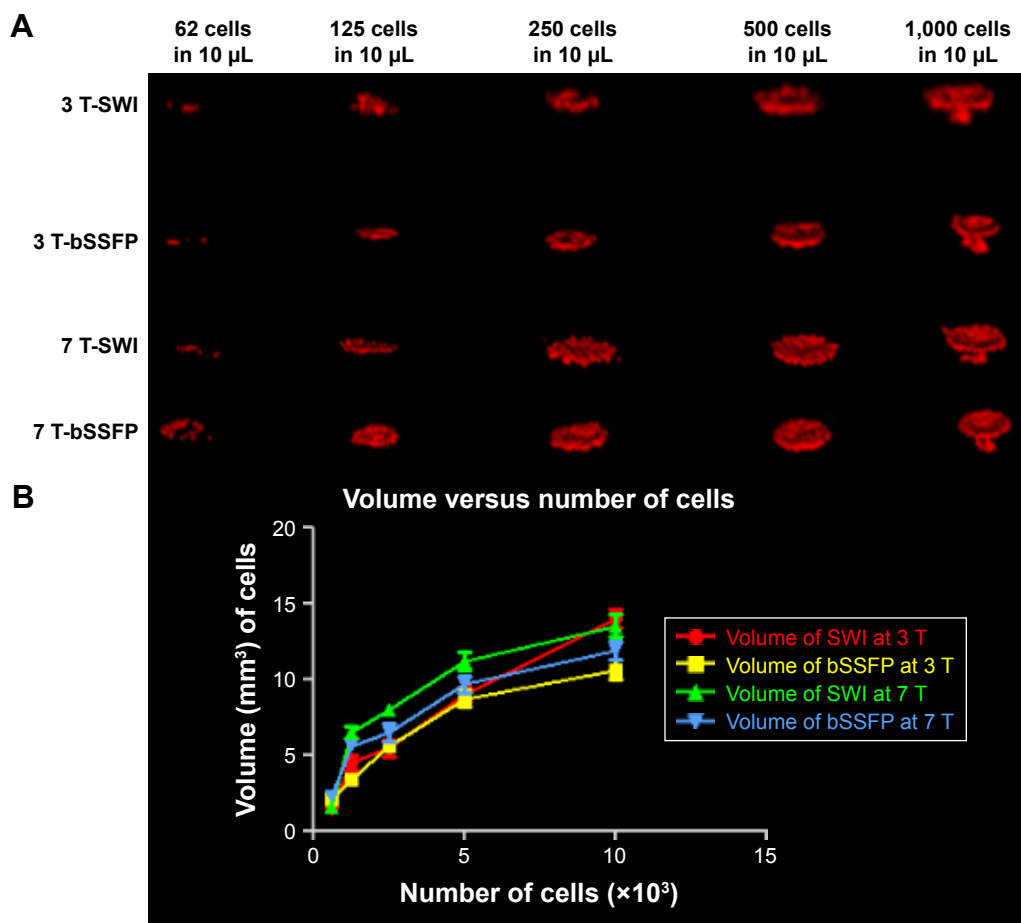


**Figure 6** (A) 3D view of manually segmented volumes of labeled cells with different concentrations on SWI and RMS combined phase-cycled bSSFP at 3 and 7 T. (B) Segmented volume versus number of cells using SWI and phase-cycled bSSFP at 3 and 7 T.

**Abbreviations:** 3D, three dimensional; bSSFP, balanced steady-state free precession; RMS, root mean square; SWI, susceptibility-weighted imaging.

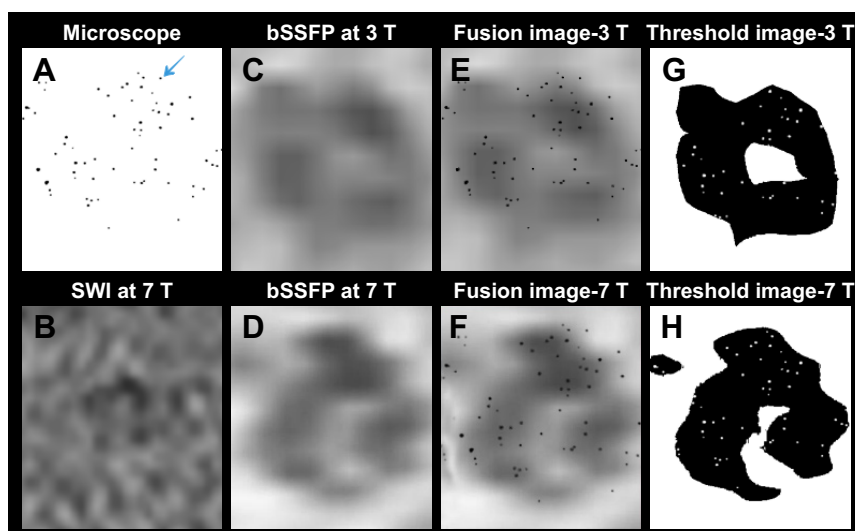


**Figure 7** Diagram showing co-registration of microscope images and MRI of the phantom with 63 cells.

**Notes:** Image registration was performed using b-spline transformation and mutual information metric provided in Elastix. (A) The microscope images of the 63 cells post-processed by ImageJ to show only the cells as dark spots. Blue arrow indicates the cells. (B) The SWI images of the 63 cells are too noisy for co-registration and overlay. (C) Zoomed 3 T RMS combined bSSFP image of the 63 cells. (D) Zoomed 7 T RMS combined bSSFP image of the 63 cells. (E) The fusion images of (A and C) after co-registration. (F) The fusion images of (A and D) after co-registration. (G) Image (E) post-processed with a threshold of 40% signal decrease. (H) Image (F) post-processed with a threshold of 40% signal decrease. More cells (51/63, 81%) are detected in 7 T images compared to 3 T images (36/63, 57%).

**Abbreviations:** bSSFP, balanced steady-state free precession; MRI, magnetic resonance imaging; RMS, root mean square; SWI, susceptibility-weighted imaging.

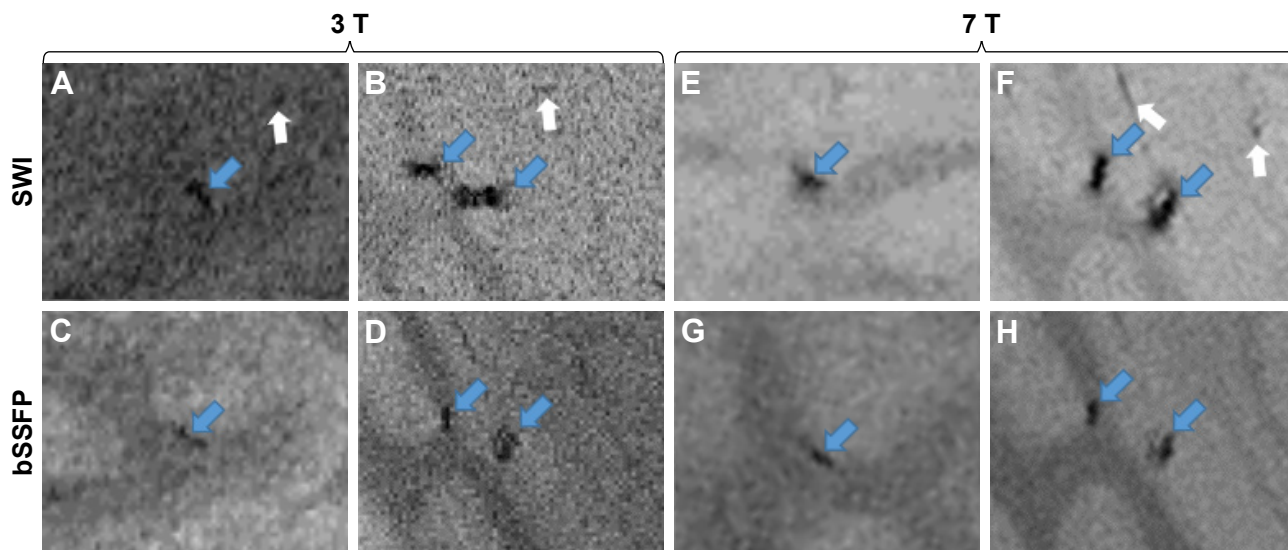


**Figure 8** Ex vivo experiment with different numbers of cells, that is,  $-100$  (A, C, E, G) and  $-1,000$  (B, D, F, H), injected into the pig brain, respectively. **Notes:** Images (A–D) were acquired at 3 T, while images (E–H) were acquired at 7 T. Images (A, B, E, and F) in the first row are SWI images, while images (C, D, G, and H) in the second row are RMS combined phase-cycled bSSFP images. The blue arrows in images (A–H) show labeled cells, while the white arrows show false-positive detection of labeled cells. **Abbreviations:** bSSFP, balanced steady state free precession; SWI, weighted imaging.

Most studies have used GRE and SWI sequences for detecting USPIO-labeled cells, by exploiting the “blooming” effect on MR phase images to accentuate the signal loss. The blooming effect has been reported to spatially extend to approximately two orders of the original size of the object.<sup>19</sup> In addition, quantitative susceptibility map may be applied for estimating the susceptibility of the source and its iron concentration.<sup>20,21</sup> However, the SNR of GRE and SWI sequences is relatively low for detecting USPIO-labeled cells with potential confounds from other susceptibility sources such as air and blood vessels. The bSSFP offers an appealing alternative to GRE/SWI for cell tracking using MRI,<sup>22,23</sup> by taking advantage of 1) the high SNR efficiency; 2) the unique T2/T1 contrast ideally suited for detecting USPIOs that primarily generate negative T2 contrast with moderate effects on T1; and 3) the strong intravoxel magnetic gradients generated by an SPIO-labeled cell that cause multiple bands emanating from the cell.<sup>24</sup> It has been shown both theoretically and experimentally that bSSFP is able to detect single cells labeled with SPIOs.<sup>22,24</sup>

In the present study, phase-cycled bSSFP offered higher SNR and CNR efficiencies than SWI for detecting USPIO-labeled cells, while effectively removing banding artifact caused by (large-scale) field inhomogeneity and susceptibility effects as well as blood flow-related artifacts. A monotonic relationship between phase-cycled bSSFP (and SWI) signal changes and cell number was also demonstrated in the present study. The disadvantage of bSSFP is banding

artifact, which requires phase-cycled measurements with lengthy scan time. We have proposed a highly efficient simultaneous multi-slice bSSFP technique<sup>25</sup> to acquire phase-cycled bSSFP images within the scan time of the standard single-phase bSSFP scan. Alternatively, an integrated SSFP technique<sup>26,27</sup> may be applied for detecting USPIO-labeled cells by removing the sensitivity of bSSFP to large-scale field variations, while maintaining similar image contrast and SNR. In future studies, both simultaneous multi-slice bSSFP and integrated SSFP may be applied for cell tracking experiment without lengthening the scan time at high and ultrahigh magnetic fields.

## Ultrahigh magnetic field for cellular imaging

Ultrahigh magnetic field is an emerging trend in neuroimaging that allows increased SNR, spatial and temporal resolutions, and enhanced sensitivity to susceptibility effects. Structural and functional MRI with a sub-millimeter spatial resolution is readily achievable at 7 T. The cell tracking results can be directly integrated with the high-resolution multi-contrast MRI to identify the fine brain structure to which the cells are delivered (eg, small blood vessels versus perivascular space). In addition, specific physiological and functional changes induced by USPIO-labeled cells can be simultaneously measured by MRI (eg, using arterial spin labeling and blood oxygenation level dependent functional MRI). The 7 T Terra MR system used in the present study is

the first FDA-approved UHF MR system. It is equipped with high order (third) shimming and the performance gradient system with a maximal strength of 80 mT/m (also installed on 3 T Prisma MR system). All developed MR pulse sequences and imaging protocols can, therefore, be directly translated to human brain imaging.

## Improved cell labeling efficiency using ferumoxytol nanocomplexes

Another challenge for existing USPIO-based cellular imaging is that the labeling efficiency of most immune or stem cells is relatively low. Ferumoxytol alone<sup>28</sup> or in combination with protamine<sup>29,30</sup> was found to not effectively label cells. Recently, self-assembling nanocomplexes by combining heparin, protamine, and ferumoxytol were introduced for efficient cell labeling with threefold increase in T2 relaxivity compared to ferumoxytol alone.<sup>4</sup> By utilizing HPF nanocomplex-labeled white blood cells (macrophages), we were able to achieve >90% labeling efficiency and demonstrate the feasibility for detecting a few tens (<100) of cells in serum-free medium and ex vivo tissue samples using phase-cycled bSSFP imaging at 7 T.

## USPIO labeling of immune cells

In the present study, we used HPF nanocomplex-labeled macrophages as a proof-of-concept of cellular MRI, which has several potential advantages. First, most existing approaches for cell tracking suffer from the loss of labeling when the cell dies. For macrophages, even when the cell dies, the nanoparticles will still be cleared by other macrophages, which means that the nanoparticles will continue to stay in the reticuloendothelial system although the USPIO concentration may vary. Second, macrophage is the end stage of the reticuloendothelial system, which means it will not divide. The USPIO labeling will not dilute to undetectable levels as the cell divides. Third, as the most plastic cells of the hematopoietic system, macrophages play an important role in many diseases related to the human immune system.<sup>31</sup> A number of macrophage-pacifying therapies have been proposed for treatment of tumor. Therefore, the proposed cell labeling and imaging of macrophages may have applications in the early diagnosis and treatment of tumor.

The central nervous system (CNS) has an immune privilege protected by the blood–brain barrier (BBB) and maintained by the glia. Nevertheless, research in the field of neuroimmunology in the past 20 years has shown that in homeostatic conditions, peripheral immune cells are able to penetrate to the deepest regions of brain without altering the

structural integrity of the BBB.<sup>32,33</sup> Peripheral white blood cells may gain access to the brain through first transmigration from the endothelial wall to the perivascular spaces and then progression across the glia limitans into the parenchyma.<sup>33</sup> In healthy brain, macrophages primarily stay within the perivascular space for performing immune surveillance and profiling their differentiation programs accordingly.<sup>34,35</sup> The second route for peripheral white blood cells to gain access to the CNS is through the blood–cerebrospinal fluid (CSF) barrier including the choroid plexus and the subarachnoid space. There is a consensus in assigning the choroid plexus as the most accessible yet selective gate for white blood cell or leukocyte transmigration into the brain.<sup>36</sup> As posited by the theory of “glymphatic system”, immune cells of CSF could have direct contact with extracellular brain proteins and solutes and, therefore, participate in their clearance or alternatively start to mount an effective immune response.<sup>37</sup> In summary, the various routes for peripheral immune cells to gain access to the CNS in homeostatic conditions open the door to deliver USPIO-labeled cells into a healthy brain without compromising the integrity of the BBB.

## Potential clinical translations

Since HPF are all FDA-approved drugs, the proposed method for cell labeling with nanocomplexes bears considerable potential for translation to human brain imaging. The proposed method may have broad clinical applications that involve cell types with a primary phagocytic phenotype. In the future, HPF nanocomplex-labeled white blood cells (eg, macrophages and monocytes) may be delivered through intravenous infusion for in vivo cellular brain imaging at 7 T. Monocytes and macrophages have a relatively long life of days with a relatively large cell body of ~20 μm, facilitating in vivo cell tracking.<sup>38</sup> Unlike other immune cells such as T-cells, monocytes and macrophages do not divide; therefore, the cell labeling would not be diluted. Tracking peripheral white blood cells into the brain in vivo may address a number of fundamental neuroscientific questions (eg, to test the theory of “glymphatic system”) and may demonstrate the route by which blood-derived leukocytes enter the CNS and circulate within the perivascular space of CSF and/or through the brain parenchyma. The proposed method may also be ideal for tracking macrophages in neoplasms and may even have therapeutic value. Recent studies have shown that macrophages exposed to ferumoxytol can inhibit the growth of subcutaneous adenocarcinomas in mice.<sup>39</sup> With the recent FDA approval of cell-based chimeric antigen receptor T cell therapy that employs genetically engineered T-cells to target

tumor cells,<sup>40</sup> we expect cell-based therapy, imaging methods, and associated labeling strategies will grow substantially in the coming years.

## Limitations of the study

The proposed cell tracking application by the phase-cycled bSSFP of HPF nanocomplex-labeled macrophages at UHF MRI has several limitations. First, it may be challenging to inject macrophages into the vein or artery, given its large size. It means that this approach may require a local injection or specific injection method to avoid these side effects. Alternatively, we may label cells with smaller size (eg, monocytes) for intravenous delivery. In view of the technology translation to clinical use, we only use the recommended clinical dosage of ferumoxytol and do not discuss the signal change caused by the concentration changes of ferumoxytol. Second, although we tried to match the imaging parameters between SWI and bSSFP at 3 and 7 T, it is still impossible to make them identical. Due to technical limitations, no histologic comparison was performed for ex vivo imaging results. Third, USPIOs are not detected directly; rather, they are detected through the use of indirect microscopic disturbances in the magnetic field. As a result, it proves challenging to correlate the MRI signal with the number of cells present, although we demonstrated a monotonic relationship between MRI signal change and cell number. Magnetic particle imaging may offer an alternative approach for detecting and quantifying USPIOs.

## Conclusion

The proposed cellular MRI with ferumoxytol nanocomplex-labeled macrophages at 7 T has a high sensitivity to detect <100 cells. Since HPF as well as 7 T Terra are FDA approved, the proposed method has great translational potential and may have broad clinical applications that involve cell types with a primary phagocytic phenotype.

## Acknowledgments

This work was supported by the US National Institute of Health (NIH) grants UH2-NS100614, R01EB014922, K25AG056594, the American Heart Association (AHA) grant 6SDG29630013, and the Shandong science and technology development plan 2015GSF118005. The authors thank Dr. Yuchuan Qiao for assistance with co-registration of the microscope image and MRI.

## Disclosure

The authors report no conflicts of interest in this work.

## References

- Korchinski DJ, Taha M, Yang R, Nathoo N, Dunn JF. Iron oxide as an MRI contrast agent for cell tracking. *Magn Reson Insights*. 2015; 8(Suppl 1):15–29.
- Makela AV, Murrell DH, Parkins KM, Kara J, Gaudet JM, Foster PJ. Cellular imaging with MRI. *Top Magn Reson Imaging*. 2016;25(5): 177–186.
- Bulte JW. In vivo MRI cell tracking: clinical studies. *AJR Am J Roentgenol*. 2009;193(2):314–325.
- Thu MS, Bryant LH, Coppola T, et al. Self-assembling nanocomplexes by combining ferumoxytol, heparin and protamine for cell tracking by magnetic resonance imaging. *Nat Med*. 2012;18(3):463–467.
- Tsuchiya S, Yamabe M, Yamaguchi Y, Kobayashi Y, Konno T, Tada K. Establishment and characterization of a human acute monocytic leukemia cell line (THP-1). *Int J Cancer*. 1980;26(2):171–176.
- Strober W. Trypan blue exclusion test of cell viability. *Curr Protoc Immunol*. 2001;Appendix 3:Appendix 3B.
- Arbab AS, Bashaw LA, Miller BR, et al. Characterization of biophysical and metabolic properties of cells labeled with superparamagnetic iron oxide nanoparticles and transfection agent for cellular MR imaging. *Radiology*. 2003;229(3):838–846.
- Bangerter NK, Hargreaves BA, Vasanawala SS, Pauly JM, Gold GE, Nishimura DG. Analysis of multiple-acquisition SSFP. *Magn Reson Med*. 2004;51(5):1038–1047.
- Yushkevich PA, Piven J, Hazlett HC, et al. User-guided 3D active contour segmentation of anatomical structures: significantly improved efficiency and reliability. *Neuroimage*. 2006;31(3):1116–1128.
- Klein S, Staring M, Murphy K, Viergever MA, Pluim JP. Elastix: a toolbox for intensity-based medical image registration. *IEEE Trans Med Imaging*. 2010;29(1):196–205.
- Daldrup-Link HE, Brasch RC. Macromolecular contrast agents for MR mammography: current status. *Eur Radiol*. 2003;13(2):354–365.
- Hoehn M, Küstermann E, Blunk J, et al. Monitoring of implanted stem cell migration in vivo: a highly resolved in vivo magnetic resonance imaging investigation of experimental stroke in rat. *Proc Natl Acad Sci U S A*. 2002;99(25):16267–16272.
- Dahnke H, Schaeffter T. Limits of detection of SPIO at 3.0 T using T2\* relaxometry. *Magn Res Med*. 2005;53(5):1202–1206.
- Kircher MF, Allport JR, Graves EE, et al. In vivo high resolution three-dimensional imaging of antigen-specific cytotoxic T-lymphocyte trafficking to tumors. *Cancer Res*. 2003;63(20):6838–6846.
- Foster-Gareau P, Heyn C, Alejski A, Rutt BK. Imaging single mammalian cells with a 1.5 T clinical MRI scanner. *Magn Res Med*. 2003;49(5): 968–971.
- Heyn C, Bowen CV, Rutt BK, Foster PJ. Detection threshold of single SPIO-labeled cells with FIESTA. *Magn Res Med*. 2005;53(2): 312–320.
- Lewin M, Carlesso N, Tung CH, et al. Tat peptide-derivatized magnetic nanoparticles allow in vivo tracking and recovery of progenitor cells. *Nat Biotechnol*. 2000;18(4):410–415.
- Shichinohe H, Kuroda S, Kudo K, et al. Visualization of the superparamagnetic iron oxide (SPIO)-labeled bone marrow stromal cells using a 3.0-T MRI—a pilot study for clinical testing of neurotransplantation. *Transl Stroke Res*. 2012;3(1):99–106.
- Liu S, Buch S, Chen Y, et al. Susceptibility-weighted imaging: current status and future directions. *NMR Biomed*. 2017;30(4).
- Buch S, Cheng YN, Hu J, et al. Determination of detection sensitivity for cerebral microbleeds using susceptibility-weighted imaging. *NMR Biomed*. 2017;30(4).
- Zheng W, Nichol H, Liu S, Cheng YC, Haacke EM. Measuring iron in the brain using quantitative susceptibility mapping and X-ray fluorescence imaging. *Neuroimage*. 2013;78:68–74.
- Heyn C, Ronald JA, Mackenzie LT, et al. In vivo magnetic resonance imaging of single cells in mouse brain with optical validation. *Magn Reson Med*. 2006;55(1):23–29.
- Foster-Gareau P, Heyn C, Alejski A, Rutt BK. Imaging single mammalian cells with a 1.5 T clinical MRI scanner. *Magn Reson Med*. 2003; 49(5):968–971.

24. Heyn C, Bowen CV, Rutt BK, Foster PJ. Detection threshold of single SPIO-labeled cells with FIESTA. *Magn Reson Med*. 2005;53(2): 312–320.
25. Wang Y, Shao X, Martin T, Moeller S, Yacoub E, Wang DJ. Phase-cycled simultaneous multislice balanced SSFP imaging with CAIPIR-INHA for efficient banding reduction. *Magn Reson Med*. 2016;76(6): 1764–1774.
26. Sun K, Xue R, Zhang P, et al. Integrated SSFP for functional brain mapping at 7T with reduced susceptibility artifact. *J Magn Reson*. 2017; 276:22–30.
27. Martin T, Wang Y, Shams R, et al. Highly Accelerated SSFP Imaging with Controlled Aliasing in Parallel Imaging and integrated-SSFP (CAIPI-iSSFP). *Invest Magn Reson Imaging*. 2017;21(4):210–222.
28. Oude Engberink RD, van der Pol SM, Dopp EA, de Vries HE, Blezer EL. Comparison of SPIO and USPIO for in vitro labeling of human monocytes: MR detection and cell function. *Radiology*. 2007;243(2): 467–474.
29. Neuwelt EA, Hamilton BE, Varallyay CG, et al. Ultrasmall superparamagnetic iron oxides (USPIOs): a future alternative magnetic resonance (MR) contrast agent for patients at risk for nephrogenic systemic fibrosis (NSF)? *Kidney Int*. 2009;75(5):465–474.
30. Janic B, Iskander A, Rad AM, Soltanian-Zadeh H, Arbab AS. Effects of ferumoxides–protamine sulfate labeling on immunomodulatory characteristics of macrophage-like THP-1 cells. *PLoS One*. 2008;3(6): e2499.
31. Wynn TA, Chawla A, Pollard JW. Macrophage biology in development, homeostasis and disease. *Nature*. 2013;496(7446):445–455.
32. Corraliza I. Recruiting specialized macrophages across the borders to restore brain functions. *Front Cell Neurosci*. 2014;8:262.
33. Owens T, Bechmann I, Engelhardt B. Perivascular spaces and the two steps to neuroinflammation. *J Neuropathol Exp Neurol*. 2008;67(12): 1113–1121.
34. Engelhardt B, Ransohoff RM. Capture, crawl, cross: the T cell code to breach the blood-brain barriers. *Trends Immunol*. 2012;33(12): 579–589.
35. Lampron A, Elali A, Rivest S. Innate immunity in the CNS: redefining the relationship between the CNS and its environment. *Neuron*. 2013; 78(2):214–232.
36. Wilson EH, Weninger W, Hunter CA. Trafficking of immune cells in the central nervous system. *J Clin Invest*. 2010;120(5):1368–1379.
37. Iliff JJ, Wang M, Liao Y, et al. A paravascular pathway facilitates CSF flow through the brain parenchyma and the clearance of interstitial solutes, including amyloid beta. *Sci Transl Med*. 2012;4(147):147ra111.
38. Handin RI, Lux SE, Stossel TP. *Blood: Principles and Practice of Hematology*. 2nd ed. Philadelphia, PA, USA: Lippincott Williams and Wilkins; 2003.
39. Zanganeh S, Hutter G, Spittler R, et al. Iron oxide nanoparticles inhibit tumour growth by inducing pro-inflammatory macrophage polarization in tumour tissues. *Nat Nanotechnol*. 2016;11(11):986–995.
40. Maude SL, Frey N, Shaw PA, et al. Chimeric antigen receptor T cells for sustained remissions in leukemia. *N Engl J Med*. 2014;371(16): 1507–1517.

## Supplementary material

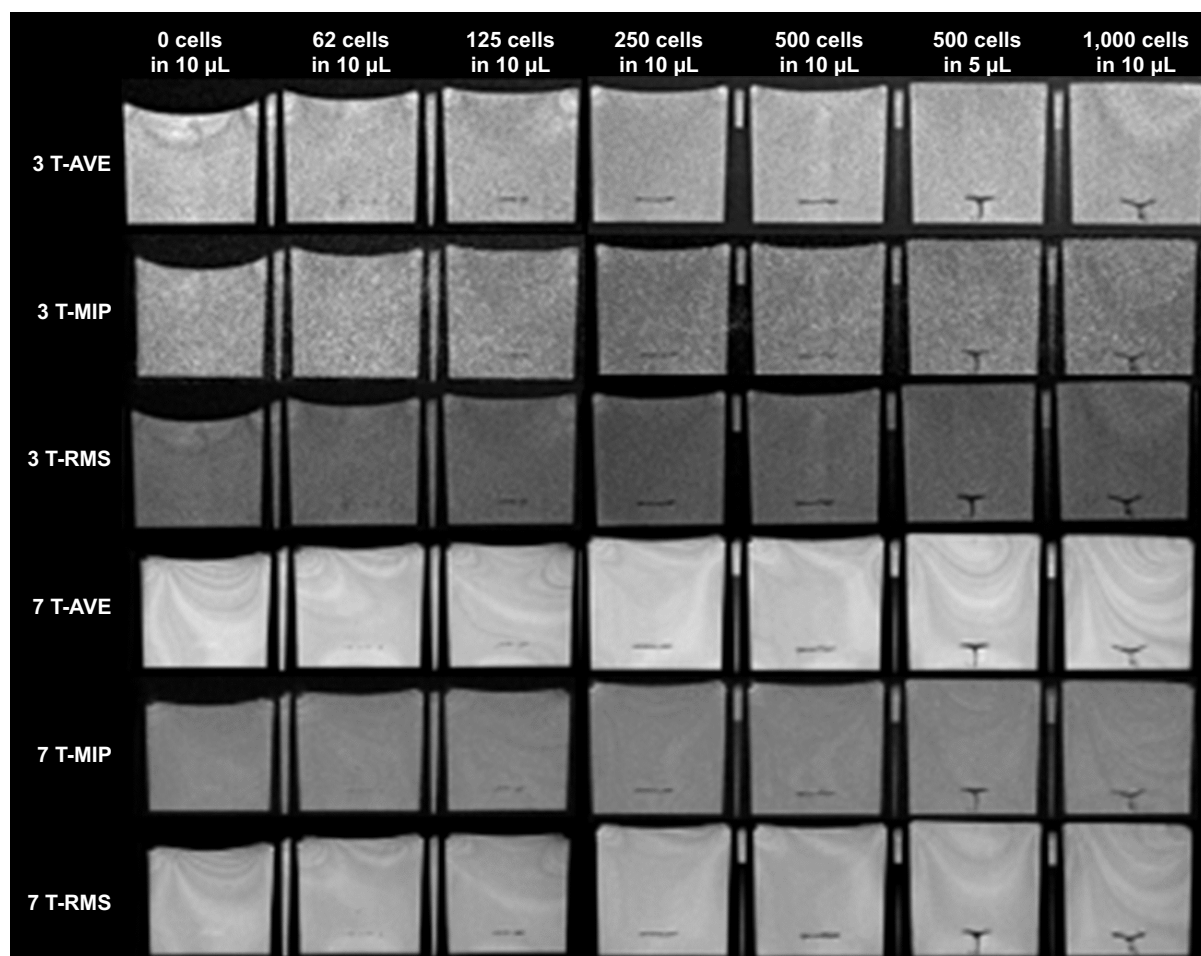


**Figure S1** AVE, MIP, and RMS combined phase-cycled bSSFP images of different concentrations of cells (0, 62, 125, 250, 500, and 1,000 cells in 10  $\mu\text{L}$  medium including 500 cells in 5  $\mu\text{L}$  medium) in the gelatin phantom.

**Note:** Phase-cycled bSSFP images were combined with three methods to minimize banding artifacts.

**Abbreviations:** AVE, average of the signal; bSSFP, balanced steady-state free precession; MIP, maximum intensity projection; RMS, root mean square.

International Journal of Nanomedicine

Dovepress

Publish your work in this journal

The International Journal of Nanomedicine is an international, peer-reviewed journal focusing on the application of nanotechnology in diagnostics, therapeutics, and drug delivery systems throughout the biomedical field. This journal is indexed on PubMed Central, MedLine, CAS, SciSearch®, Current Contents®/Clinical Medicine,

Journal Citation Reports/Science Edition, EMBase, Scopus and the Elsevier Bibliographic databases. The manuscript management system is completely online and includes a very quick and fair peer-review system, which is all easy to use. Visit <http://www.dovepress.com/testimonials.php> to read real quotes from published authors.

Submit your manuscript here: <http://www.dovepress.com/international-journal-of-nanomedicine-journal>